A Priori Analyses of Three Subgrid-Scale Models for One-Parameter Families of Filters[1]

Dr. C. David Pruett
Department of Mathematics
James Madison University
Harrisonburg, Virginia, USA

Dr. Nikolaus A. Adams
Institute of Fluid Dynamics
ETH Zürich
Zürich, Switzerland

Abstract

The decay of isotropic turbulence in a compressible flow is examined by direct numerical simulation (DNS). *A priori* analyses of the DNS data are then performed to evaluate three subgrid-scale (SGS) models for large-eddy simulation (LES): a generalized Smagorinsky model ($M1$) [*J. Fluid Mech.*, **238**, 1 (1992)], a stress-similarity model ($M2$) [*J. Fluid Mech.*, **275**, 83 (1994)], and a gradient model ($M3$) [*Theoret. Comput. Fluid Dynamics*, **8**, 309 (1996)]. The models exploit one-parameter second- or fourth-order filters of Pade type, which permit the cutoff wavenumber k_c to be tuned independently of the grid increment Δx. The modeled (M) and exact (E) SGS-stresses are compared component-wise by correlation coefficients of the form $C(E, M)$ computed over the entire three-dimensional fields. In general, $M1$ correlates poorly against exact stresses ($C < 0.2$), $M3$ correlates moderately well ($C \approx 0.6$), and $M2$ correlates remarkably well ($0.8 < C < 1.0$). Specifically, correlations $C(E, M2)$ are high provided the grid and test filters are of the same order. Moreover, the highest correlations ($C \approx 1.0$) result whenever the grid and test filters are *identical* (in both order and cutoff). Finally, present results reveal the *exact* SGS stresses obtained by grid filters of differing orders to be only moderately well correlated. Thus, in LES the model should not be specified independently of the filter.

Keywords: large-eddy simulation, subgrid-scale modeling, isotropic turbulence, compressible flow, digital filtering

1 Introduction

By definition, direct numerical simulation (DNS) is the numerical solution of the Navier-Stokes equations without recourse to empirical models. In concept, the fluid motions are resolved down to the Kolmogorov wavenumber k_η, at which eddies succumb to viscous dissipation. In general, the computational workload for fully-resolved DNS scales as Re^3, where Re is the Reynolds number. For the complex, high-Reynolds-number flows of engineering interest, the computational requirements of DNS are staggering and prohibitive. Consequently, large-eddy simulation (LES) remains an attractive (and necessary) alternative.

In contrast to DNS, LES is based on a decomposition of the flow-field variables into resolved and unresolved (subgrid) scales. The decomposition is effected by a spatial *grid* filtering operation with an associated cutoff wavenumber k_c. The grid-filtered Navier-Stokes equations incorporate the subgrid-scale (SGS) stress tensor τ_{kl}, which quantifies the interactions between the smaller ($k \geq k_c$) and larger ($k < k_c$) scales of motion. The larger scales are resolved in space and time on a suitable computational grid; however, the SGS stresses are modeled or otherwise approximated.

The relationship between DNS and (idealized) LES is illustrated in Fig. 1, which presents the Kolmogorov energy spectrum. The inertial range of the spectrum is characterized by energy decay at the rate $E(k) \sim k^{-5/3}$. By implication, τ_{kl} varies with the cutoff k_c; that is, $\tau_{kl} = \tau_{kl}(k_c)$. For DNS, $k_c = k_\eta$ and, for all practical purposes, $\tau_{kl}(k_\eta) = 0$.

A general criticism of LES [1] is that the truncation errors of the numerical method often contaminate the SGS dissipation. There is growing realization (e.g., Vasilyev et al. [2]) that this situation can be avoided by independent specification of the grid resolution Δx^* and the wavenumber cutoff k_c^*. (Throughout this work, asterisks denote dimensional quantities.) In our view, k_c^* should be specified on the basis of physical considerations; that is, k_c^* should lie in the inertial range of the Kolmogorov spectrum (Fig. 1). On the other hand, Δx^* should be determined by numerical considerations; that is, by the grid resolution necessary to resolve the smallest eddies (those of wavelength $\lambda_c^* = 2\pi/k_c^*$) *for the numerical scheme of choice.*

2

For example, spectral, sixth-order, fourth-order, and second-order difference approximations typically require 2, 10, 16, and 32 gridpoints, respectively, per wavelength of the smallest resolved scale. If we define the dimensionless wavenumber $\alpha \equiv k^* \Delta x^*$, then $\alpha_c \equiv k_c^* \Delta x^*$ defines the dimensionless filter cutoff. It is highly desirable, therefore, to exploit continuously tunable filters, whose cutoffs α_c are not "hard-wired" to the grid resolution. For this purpose, we adapt one-parameter families of filters of Pade type, as described in Lele [3].

Our present work parallels the experimental investigations of Liu et al. [4] and the computational work of Vreman et al. [5]. Each paper evaluates the potential of candidate SGS models by means of *a priori* analyses. (The latter work also performs *a posteriori* analyses.) In their ground-breaking experiment, Liu et al. [4] investigated the structure of turbulence in the far field of an axisymmetric water jet by means of particle-displacement velocimetry. By planar filtering of the velocity data, they reconstructed (2D slices) of three components of the exact SGS-stress tensor and correlated various modeled stresses against their exact counterparts. To our knowledge, their experiment represents the first *a priori* analysis conducted with experimental rather than computational data. Two of the models considered by Liu et al. [4] were the standard (incompressible) Smagorinsky model and a stress-similarity model. In Vreman et al. [5], three candidate SGS models (and their dynamic counterparts) were evaluated by both *a priori* and *a posteriori* analyses, using data obtained by DNS of a weakly compressible turbulent mixing layer. Specifically, they examined Smagorinsky, similarity, and gradient [6, 7] models.

In the present paper, we evaluate, for the case of decaying isotropic turbulence, the three models considered by Vreman et al. [5]. Our evaluation is limited to *a priori* analysis only and has a different focus than the work of Vreman et al. [5]. Whereas, they exploit a top-hat filter with a fixed filter width (twice the grid increment) and focus on the SGS models, we exploit Pade-type filters and focus specifically on the effects of the filter. In particular, we examine the effects of the cutoff and the order property of the filter on the fidelity of the models.

The next section discusses our two candidate filters: second- and fourth-order filters of

Pade type with continuous variation of the cutoff α_c. In Section 3, we present the unfiltered and filtered compressible Navier-Stokes equations, which serve as the governing systems for DNS and LES, respectively. Section 4 describes the three SGS models to be considered: the generalized Smagorinsky model of Erlebacher et al. [8], the stress-similarity model of Liu et al. [4], and the generalized Clark model of Vreman et al. [7]. Section 5 presents parameters of the test flow: decaying isotropic turbulence. The *a priori* analysis is presented in Section 6. In particular, we present correlations between the exact SGS-stress components and their modeled counterparts. A brief discussion of the results is presented in Section 7, and conclusions are offered in Section 8.

2 One-Parameter, Low-Pass Filters

Many types of spatial, linear, low-pass filters can be used for LES, the most popular being top-hat, Gaussian, and spectral filters. The properties of admissible filters can be found in many sources, including Erlebacher et al. [8].

Following Lele [3], we consider one-parameter families of filters of Pade type that are both symmetric and positive semidefinite. The positivity of these filters ensures that the SGS-stress tensor is realizable in the sense of Vreman et al. [9]. A filter is best understood in terms of its transfer function, which depicts its effect on modes of wavenumber α. The transfer functions of a family of second-order Pade filters are shown in Fig. 2 for selected values of the cutoff α_c. The dissipation imposed by the filter varies continuously over the range $0 < \alpha_c \leq \pi$, decreasing with increasing α_c. Specifically $\alpha_c = \pi$ turns off the filter, $\alpha_c = \pi/2$ results in the discrete top-hat filter (with weights at adjacent nodes of [1/4, 1/2, 1/4]), and $\alpha_c \approx 0$ results in extreme dissipation. In general, one-parameter filters are advantageous relative to fixed-width filters in that α_c can be adjusted so as to specify k_c independently of Δx. For some purposes, we will also exploit a one-parameter, fourth-order Pade filter with the same parameter range. Details of the both filters are relegated to the Appendix.

For our present purposes, multidimensional filtering is accomplished by filtering succes-

4

sively in each coordinate dimension. The same cutoff is exploited in each dimension.

3   Governing Equations

For DNS, the Navier-Stokes equations are solved numerically on a grid sufficiently fine to resolve all energetic scales of motion.

3.1   Compressible Navier-Stokes Equations

In tensor notation, the dimensionless equations governing the evolution of an ideal gas in time t and Cartesian space $\mathbf{x} = [x_1, x_2, x_3]$ are

$$
\begin{aligned}
\frac{\partial \rho}{\partial t} + \frac{\partial (\rho u_k)}{\partial x_k} &= 0 \\
\frac{\partial (\rho u_k)}{\partial t} + \frac{\partial (\rho u_k u_l)}{\partial x_l} &= -\frac{\partial p}{\partial x_k} + \frac{1}{Re}\frac{\partial \sigma_{kl}}{\partial x_l} \\
\frac{\partial (E_T)}{\partial t} + \frac{\partial [(E_T + p)u_k]}{\partial x_k} &= \frac{\partial h_k}{\partial x_k} + \frac{1}{Re}\frac{\partial (u_l \sigma_{kl})}{\partial x_k}
\end{aligned}
\tag{1}
$$

where

$$
\begin{aligned}
E_T &= \rho\left(e + \frac{u_k u_k}{2}\right) \\
e &= \frac{T}{\gamma(\gamma - 1)M^2} \\
h_k &= \frac{\mu}{(\gamma - 1)M^2 Pr Re}\frac{\partial T}{\partial x_k}
\end{aligned}
\tag{2}
$$

and repeated indices imply summation. Here, ρ, p, T, e, E_T, μ, and κ are density, thermodynamic pressure, absolute temperature, specific internal energy, total energy, dynamic viscosity, and thermal conductivity, respectively, and $\mathbf{u} = [u_1, u_2, u_3]$ is the velocity vector. The quantities above have been rendered dimensionless by the choice of a reference length scale L^* and suitable reference values (denoted by subscript "r") as follows:

$$
\begin{aligned}
t &= t^* u_{\mathrm{r}}^* / L^* & x_k &= x_k^* / L^* \\
T &= T^* / T_{\mathrm{r}}^* & u_k &= u_k^* / u_{\mathrm{r}}^* \\
\rho &= \rho^* / \rho_{\mathrm{r}}^* & p &= p^* / (\rho_{\mathrm{r}}^* u_{\mathrm{r}}^{*2}) \\
\mu &= \mu^* / \mu^*(T_{\mathrm{r}}^*) & \kappa &= \kappa^* / \kappa^*(T_{\mathrm{r}}^*) \\
e &= e^* / u_{\mathrm{r}}^{*2} & E_t &= E_t^* / (\rho_{\mathrm{r}}^* u_{\mathrm{r}}^{*2})
\end{aligned}
\tag{3}
$$

From the nondimensionalizations above, four dimensionless parameters arise: the Reynolds number, the Mach number, the Prandtl number, and the ratio of specific heats. These are defined, respectively, as follows:

$$
\begin{aligned}
Re &= \frac{\rho_{\mathrm{r}}^* u_{\mathrm{r}}^* L^*}{\mu_{\mathrm{r}}^*} \\
M &= \frac{u_{\mathrm{r}}^*}{\sqrt{\gamma R^* T_{\mathrm{r}}^*}} \\
Pr &= \frac{C_p^* \mu_{\mathrm{r}}^*}{\kappa_{\mathrm{r}}^*} \\
\gamma &= \frac{C_p^*}{C_v^*}
\end{aligned}
\tag{4}
$$

Here, C_p^* and C_v^* are the specific heats at constant pressure and constant volume, respectively, and R^* is the ideal gas constant. Throughout this work, we presume the constant values $\gamma = 1.4$ and $Pr = 0.7$. The viscous stress tensor σ_{kl} is defined

$$
\sigma_{kl} = 2\mu S_{kl} - \frac{2}{3}\mu D \delta_{kl}
\tag{5}
$$

where δ_{kl} is the Kronecker delta, $D = \frac{\partial u_k}{\partial x_k}$ is the compressible dilatation, and S_{kl} is the symmetric strain-rate tensor defined as

$$
S_{kl} = \frac{1}{2}\left(\frac{\partial u_k}{\partial x_l} + \frac{\partial u_l}{\partial x_k} \right)
\tag{6}
$$

Equations 1 describe the conservation of mass, momentum, and energy, respectively. The governing system is closed by imposing an equation of state for an ideal gas, namely

$$
p = \frac{\rho T}{\gamma M^2} = (\gamma - 1)\rho e
\tag{7}
$$

The variation of μ with respect to T is modeled by Sutherland's law, and $\kappa = \mu / Pr$.

3.2 Favre-Filtered Navier-Stokes Equations

For LES of compressible flow, density-weighted (Favre) filtering arises naturally from the use of conservative variables. For example, the Favre-filtered velocity components, denoted by tildes, are given by

$$\tilde{u}_k = \frac{\overline{\rho u_k}}{\bar{\rho}}$$

$$(\bar{\rho}\tilde{u}_k = \overline{\rho u_k}) \tag{8}$$

The Favre-filtered continuity equation is form invariant; that is,

$$\frac{\partial \bar{\rho}}{\partial t} + \frac{\partial(\bar{\rho}\tilde{u}_k)}{\partial x_k} = 0 \tag{9}$$

as is the filtered equation of state $\bar{p} = \bar{\rho}\tilde{T}/(\gamma M^2)$. However, the momentum equation acquires the following filtered form:

$$\frac{\partial(\bar{\rho}\tilde{u}_k)}{\partial t} + \frac{\partial(\bar{\rho}\tilde{u}_k\tilde{u}_l)}{\partial x_l} = -\frac{\partial \bar{p}}{\partial x_k} + \frac{1}{Re}\frac{\partial \bar{\sigma}_{kl}}{\partial x_l} + \frac{\partial \tau_{kl}}{\partial x_l} \tag{10}$$

where τ_{kl} is the SGS-stress (or the residual-stress) tensor. For compressible flow, the residual-stress tensor assumes the form

$$\tau_{kl} = \bar{\rho}(\tilde{u}_k\tilde{u}_l - \widetilde{u_k u_l}) \tag{11}$$

As written, Eq. 10 is exact; however, in practice it becomes inexact because $\bar{\sigma}_{kl}$, being unavailable, is usually approximated from $\tilde{S}_{kl}$ and $\tilde{\mu}$, with residual stresses due to their nonlinear interactions being neglected. Following Erlebacher et al. [8], an alternate form of the dimensionless grid-filtered energy equation is

$$\frac{\partial \bar{p}}{\partial t} + \frac{\partial(\bar{p}\tilde{u}_k)}{\partial x_k} = -(\gamma - 1)\bar{p}\tilde{D} + \frac{1}{M^2 Pr Re}\frac{\partial}{\partial x_k}\left(\overline{\mu\frac{\partial T}{\partial x_k}}\right) + \frac{\gamma - 1}{Re}\bar{\Phi} + \frac{1}{\gamma M^2}\frac{\partial Q_k}{\partial x_k} \tag{12}$$

where the dissipation function is

$$\Phi = 2\mu S_{kl}\frac{\partial u_k}{\partial x_l} - \frac{2}{3}\mu D^2 \tag{13}$$

and the residual heat-flux vector is

$$Q_k = \bar{\rho}(\tilde{u}_k\tilde{T} - \widetilde{u_k T}) \tag{14}$$

7

Equation 12 is inexact because it has been derived by neglecting certain pressure-velocity terms, and because, in practice, the term $\overline{\mu \frac{\partial T}{\partial x_k}}$ is typically approximated from the resolved scales.

4 Subgrid-Scale Stress (SGS) Models

We consider three residual-stress models, denoted $M1$, $M2$, and $M3$, as described, respectively, below.

4.1 Generalized Smagorinsky Model ($M1$)

A generalization of the Smagorinsky model to compressible flow is presented in Erlebacher et al. [8], which we adapt as follows. Let MR_{kl} denote the modeled residual-stress tensor such that

$$MR_{kl} = \mu_T(\tilde{S}_{kl} - \frac{1}{3}\tilde{D}\delta_{kl}) \tag{15}$$

where $\tilde{S}_{ij}$ is the resolved-scale strain-rate tensor, and μ_T is the eddy viscosity defined as

$$\mu_T = 2C_R\Delta^2\bar{\rho}|\tilde{S}| \quad ; \quad |\tilde{S}| = \sqrt{\tilde{S}_{kl}\tilde{S}_{kl}} \tag{16}$$

Here, C_R is a model constant, and Δ is a characteristic length scale related to the grid spacing. Typically $\Delta = \sqrt{\Delta x^2 + \Delta y^2 + \Delta z^2}$. Similarly, the modeled residual heat-flux vector MQ_k is given by

$$MQ_k = C_q\Delta^2\bar{\rho}|\tilde{S}|\frac{\partial\tilde{T}}{\partial x_k} \tag{17}$$

where C_q is a model constant related to C_R through the turbulent Prandtl number Pr_T.

4.2 Scale-Similarity Model ($M2$)

On the basis of their experimental observations, Liu et al. [4] propose (for incompressible flow) the simple stress-similarity model

$$\tau_{kl} \approx c_L\mathcal{L}_{kl} \tag{18}$$

where c_L is a constant, and $\mathcal{L}_{kl}$ is the resolved-turbulent-stress tensor. A computable quantity, $\mathcal{L}_{kl}$ is extracted from the resolved fields by applying a second filter, termed the *test* filter and denoted by a hat. Specifically,

$$\mathcal{L}_{kl} = \hat{\tilde{u}}_k \hat{\tilde{u}}_l - \widehat{\tilde{u}_k \tilde{u}_l} \tag{19}$$

In general, the cutoffs associated with the grid and test filters may be different. Bardina's [10] model is the special case of Eq. 18 for which $c_L = 1$ and $r = 1$, where $r = \hat{\Delta}/\Delta$, and $\hat{\Delta}$ and Δ are the filter widths associated with the test and grid filters, respectively.

For compressible flows, attempts to distinguish Favre grid- and test-filtered quantities result in cumbersome notation. Therefore, we adopt the simplifying convention that, for any twice-filtered quantity, the first and second filtering operations are presumed to correspond to the test and grid filters, respectively, which may have different cutoffs. Following this convention, the resolved-turbulent-stress tensor is

$$\mathcal{L}_{kl} = \bar{\rho}(\hat{\tilde{u}}_k \hat{\tilde{u}}_l - \widehat{\tilde{u}_k \tilde{u}_l}) \tag{20}$$

and its thermal counterpart is

$$q_k = \bar{\rho}(\hat{\tilde{u}}_k \hat{\tilde{T}} - \widehat{\tilde{u}_k \tilde{T}}) \tag{21}$$

4.3 Generalized Clark Model ($M3$)

Using Taylor-series expansions of the filtered velocity fields in terms of the unfiltered velocities, Vreman et al. [7] derive the gradient model

$$\tau_{kl} = -\frac{1}{12}\Delta^2 \bar{\rho}\frac{\partial \tilde{u}_k}{\partial x_j}\frac{\partial \tilde{u}_l}{\partial x_j} + O(\Delta^4) \tag{22}$$

(The negative sign is included for consistency with our definition of the residual stress (Eq. 11)). Their model generalizes that of Clark et al. [6] to compressible flows. Criticism of the use of Taylor expansions by Love [11] has been addressed in Vreman et al. [7]. Here, our purpose is not to defend or refute the Taylor-series approach, but simply to evaluate the proposed model by *a priori* analysis.

5 Test Case: Decaying Isotropic Turbulence

We consider the decay of an isotropic turbulent compressible flow. Specifically, the test case corresponds approximately to case *ife96* of Blaisdell et al. [12], whose parameter values are restated below for completeness.

$$
\begin{aligned}
Re &= 166. \\
M &= 1.0 \\
T_\infty^* &= 300 \text{ K}
\end{aligned}
\tag{23}
$$

where

$$
\begin{aligned}
\rho_{\text{r}}^* &= \rho_0^* \\
u_{\text{r}}^* &= c_0^* = \sqrt{\gamma R^* T_0^*} \\
T_{\text{r}}^* &= T_0^*
\end{aligned}
\tag{24}
$$

and the subscript "0" refers to spatially averaged values at the initial time. For reasons of computational efficiency, the computational domain is a cube of edge length 2π, with periodic boundary conditions in each coordinate dimension. The flow is initialized with the top-hat energy spectrum shown by solid line in Fig. 3, for which the phases are prescribed randomly. Whereas Blaisdell et al. [12] exploits a power law for the viscosity model, as mentioned previously, we employ Sutherland's law. As a consequence, some of our initial parameters differ marginally from those published in Blaisdell et al. [12]. The initial turbulent Mach number $M_t = \sqrt{<u_k'' u_k''>}/\sqrt{\gamma <p> / <\rho>} = 0.7$. Here, angle brackets denote volume averages over the entire domain (e.g., $<u> = \frac{\int_D u\,dV}{V}$), and $u_k'' = u_k - <\rho u_k> / <\rho>$. (Throughout this work, volume averages are computed by multidimensional trapezoid rule, which is spectrally accurate whenever the fields are spatially periodic). The flow is then allowed to evolve without further forcing. The temporal evolution of total kinetic energy $TKE = 0.5 <\rho u_k'' u_k''>$ and turbulent Mach number M_t are shown in Figs. 4 and 5, respectively. Energy spectra $E(k)$ at selected times are compared with the initial spectrum

in Fig. 3. Here, $k = |\mathbf{k}| = \sqrt{k_1^2 + k_2^2 + k_3^2}$, where $\mathbf{k} = [k_1, k_2, k_3]$ is the wavenumber vector in Fourier space.

6 DNS: *A Priori* Testing

The governing equations (Eq. 1) are solved by efficient pseudospectral methods using the algorithm developed by Obrist [13] for his Diploma thesis at ETH under the direction of the second author. The uniformly-spaced computational grid uses 96 points (48 Fourier modes) in each coordinate dimension. Because the flow is well resolved at the 96^3 resolution for the particular parameter values of interest, no explicit dealiasing is necessary (nor is it desirable). Time is advanced fully explicitly by the third-order low-storage Runge-Kutta method of Williamson [14].

As noted in Blaisdell et al. [12], the Reynolds number of the simulation is insufficiently high to result in a distinct inertial subrange with a characteristic -5/3 power-law decay. The temporal evolution of the spectrum of the present simulation is shown in Fig. 3. All analyses are performed at dimensionless time $t = 1.51$. For completeness, Figs. 6, 7, and 8 show the temporal evolution of the turbulent Reynolds number Re_T, the Taylor microscale λ_{11}, and the Taylor microscale Reynolds number Re_λ, which are defined, respectively, as follows:

$$
\begin{aligned}
Re_T &= Re\frac{<\rho u_k'' u_k''>^2}{\epsilon \tilde{\mu}} \\
\tilde{\mu} &= \frac{<\rho\mu>}{<\rho>} \\
\epsilon &= \frac{1}{Re} < \sigma_{ij}\frac{\partial u_k''}{\partial x_l} >
\end{aligned}
\tag{25}
$$

$$
\lambda_{kl}^2 = \frac{< u_k' u_k' >}{< (\frac{\partial u_k'}{\partial x_l})^2 >}
\tag{26}
$$

$$
Re_\lambda = Re < \rho > q\lambda_{11}\tilde{\mu}
\tag{27}
$$

11

(k, l)	λ_{kl}
(1,1)	0.3579
(1,2)	0.2925
(1,3)	0.2949
(2,1)	0.2862
(2,2)	0.3600
(2,3)	0.2928
(3,1)	0.2882
(3,2)	0.2922
(3,3)	0.3566

Table 1: Taylor-microscale components at dimensionless time $t = 1.51$.

$$q = \left[\frac{< \rho u_k'' u_k'' >}{< \rho >} \right]^{1/2}$$

Note that q is a turbulent velocity scale, for which $TKE = q^2/2$, and that ϵ is the turbulent dissipation rate. Like Blaisdell et al. [12] we observe two distinct microscales. The diagonal components of λ_{kl} are consistent as are the off-diagonal components, as shown in Table 1. In general, the diagonal components are larger by 20-40 percent. Also as observed by Blaisdell et al. [12], the microscale diminishes at first and then grows gradually. For comparisons with the results of Blaisdell et al. [12], for which time is typically given in units $t\epsilon_0/(TKE)_0$, we note that our dimensionless time should be scaled by a factor of approximately two.

Fig. 9 presents contours of constant τ_{11} in an arbitrarily selected $x - y$ plane that corresponds to $z = 0.6545$. The residual-stress component is computed exactly by grid-filtering the DNS results according to Eq. 11. Fig. 9 further compares the exact residual stress component with contours of the corresponding components of the Smagorinsky ($M1$, Eq. 15), similarity ($M2$, Eq. 18), and generalized Clark models ($M3$, Eq. 22), respectively. For $M2$, which requires twice filtered quantities, the cutoff values for the grid and test filters are $\alpha_\xi = \pi/2$ and $\alpha_c = 0.93$, respectively. Fig. 9 clearly reveals model $M2$ to be much more highly correlated to the exact residual stress (E) than either $M1$ or $M3$.

The numerical values of these correlations are summarized in Table 2 for all components of τ_{kl}. In particular, Table 2 presents correlations of the form $C(E, M)$ between the exact

$(1.91,\pi/2)$	$C(E,M1)$	$C(E,M2)$	$C(E,M3)$
τ_{11}	0.066	0.977	0.619
τ_{12}	0.182	0.975	0.650
τ_{13}	0.125	0.978	0.546
τ_{22}	0.081	0.976	0.609
τ_{23}	0.113	0.978	0.540
τ_{33}	0.214	0.980	0.412
$(\pi/2,0.93)$	$C(E,M1)$	$C(E,M2)$	$C(E,M3)$
τ_{11}	0.067	0.910	0.474
τ_{12}	0.183	0.906	0.518
τ_{13}	0.116	0.913	0.432
τ_{22}	0.082	0.908	0.461
τ_{23}	0.102	0.913	0.427
τ_{33}	0.199	0.921	0.314

Table 2: Correlations between exact (E) residual-stress fields τ_{kl} and their modeled (M) counterparts, for case of differing grid and test filters, whose respective parameters α_c are provided in upper left box of each block.

(E) and modeled (M) residual-stress fields for the three models under consideration. Here, we define the correlation coefficient C between any two fields u and v in the customary way as follows:

$$C(u,v) = \frac{<uv> - <u><v>}{[(<u^2> - <u>^2)(<v^2> - <v>^2)]^{1/2}} \qquad (28)$$

In general, we observe poor correlations (typically $C < 0.2$) for $M1$, moderately high correlations ($C \approx 0.6$) for $M3$, and remarkably high correlations ($C > 0.9$) for $M3$. Two filtering operations are required to evaluate $M2$. Thus, the two values that appear in the upper left box of each block of Table 2 correspond to the respective cutoff values for the grid and test filters.

Fig. 10 and Table 3 present similar results for the residual-stress components Q_k (Eq. 14) with their modeled $(M1,M2)$ counterparts MQ_k (Eq. 17) and q_k (Eq. 21), respectively. The same levels of correlations observed for components of the SGS-stress tensor are observed also for the thermal stresses.

It is well known that scalar eddy viscosity models (e.g., $M1$) do not perform well in

$(1.91, \pi/2)$	$C(E, M1)$	$C(E, M2)$
Q_1	0.106	0.977
Q_2	0.109	0.976
Q_3	0.236	0.974
$(\pi/2, 0.93)$	$C(E, M1)$	$C(E, M2)$
Q_1	0.104	0.912
Q_2	0.110	0.911
Q_3	0.213	0.912

Table 3: Correlations between exact (E) energy residual fields Q_k and their modeled (M) counterparts, for case of differing grid and test filters, whose respective parameters α_c are provided in upper left box of each block.

anisotropic flows (e.g., Compton and Eaton [15]) because the shear stress and the mean strain are misaligned. However, the component-wise variation of the correlations $C(E, M1)$ in Tables 2 and 3 comes initially as a surprise. For isotropic turbulence, one expects the correlations to be nearly the same across all components. Statistical isotropy, however, does not imply instantaneous isotropy. Numerical experimentation with different random initial conditions and a priori analyses at different snapshots in time reveal these variations to be manifestations of instantaneous anisotropy. On the other hand, the similarity model $(M2)$ appears relatively insensitive to anisotropy.

Liu et al. [4] found Bardina's [10] model to yield the highest correlation coefficients. Accordingly, Fig. 11 presents contours of the exact (E) and similarity $(M2)$ modeled (2,3) components of the residual-stress tensor for the case in which the grid and test filters are identical, each with $\alpha_c = \pi/2$. In this case, the correlation $C(E, M2)$ attains a surprisingly high value, in excess of 0.99. Table 4 below summarizes the correlation data for various values of the cutoff α_c, which is given in the upper left box of each block in the table. The correlation coefficients of the form $C(E, M2)$ range from a low of 0.86, for an extremely dissipative filter, to 0.999, for a very mild filter. As expected, the less dissipative the filter (i.e., the higher k_c), the higher the correlation coefficient. In addition to correlation coefficients, Table 4 also indicates the ranges (maxima and minima) of the exact and modeled residual stresses. From these extrema, we make two important observations. First, the magnitudes of the

components of the *exact* residual-stress tensor τ_{kl} depend significantly on the value of the cutoff α_c. Second, whenever identical grid and test filters are exploited, τ_{kl} is apparently well approximated by Eq. 18 with $c_L \approx 1.0$, provided the filter is not too dissipative. Tables 2 and 4 reveal that the fidelity of all three models appears to deteriorate as the filter becomes highly dissipative (although the correlations for $M1$ are so poor that any effect due to filter tuning is difficult to assess).

To provide additional insight, Table 5 presents correlations of the form $C(E, M)$ for the case where the grid filter is of fourth order, as discussed in Section 2. For $M2$ the test filter is of second order, so that the grid and test filters are of differing orders. The values shown in the upper left box of each block of Table 5 correspond to the cutoff values α_c for the grid and test filters, respectively. In general, component-wise correlations for the generalized Smagorinsky model appear to drop below their previously low values, as suggested by a comparison of Tables 2 and 5. Moreover, correlations of the type $C(E, M2)$ drop dramatically to range from 0.5 to 0.7 depending upon the values of the grid- and test-filter cutoffs. The poorest correlations for $M2$ arise when the respective cutoffs are different. Curiously, $M3$ correlates as well or better for a fourth-order grid filter as it did for a second-order grid filter. This may suggest that the fourth-order term in Eq. 22 is significant.

Finally, we consider the effect of the order property of the grid filter on the *exact* residual-stress tensor. Figure 12 compares the exact (2,2) component of τ_{kl} for grid filters of different orders and cutoffs. The first grid filter is of second order with $\alpha_c = 1.16$; the second is of fourth order with $\alpha_c = 1.71$. Contours are displayed at $z = 0.6545$. Clearly, the stress distribution is grid-filter dependent. To quantify this dependence, Table 6 presents correlation coefficients of the form $C(E2, E4)$, where $E2$ and $E4$ refer to exact quantities computed by second- and fourth-order grid filtering, respectively. All components show the same level of correlation, nominally 0.54. We conclude that the *exact* residual stresses depend on the selection of the grid filter in both their distribution and their scale.

$\alpha_c = 2.21$	$C(E, M2)$	$E_{\max}$	$E_{\min}$	$M2_{\max}$	$M2_{\min}$
τ_{11}	0.997	0.112E-02	-.654E-02	0.896E-03	-.572E-02
τ_{12}	0.997	0.315E-02	-.288E-02	0.271E-02	-.247E-02
τ_{13}	0.997	0.348E-02	-.291E-02	0.298E-02	-.246E-02
τ_{22}	0.997	0.954E-03	-.728E-02	0.782E-03	-.614E-02
τ_{23}	0.997	0.270E-02	-.225E-02	0.240E-02	-.200E-02
τ_{33}	0.997	0.613E-03	-.583E-02	0.433E-03	-.489E-02
$\alpha_c = \pi/2$	$C(E, M2)$	$E_{\max}$	$E_{\min}$	$M2_{\max}$	$M2_{\min}$
τ_{11}	0.992	0.00	-.161E-01	0.00	-.125E-01
τ_{12}	0.992	0.772E-02	-.648E-02	0.620E-02	-.512E-02
τ_{13}	0.993	0.847E-02	-.621E-02	0.653E-02	-.469E-02
τ_{22}	0.992	0.00	-.167E-01	0.00	-.122E-01
τ_{23}	0.993	0.664E-02	-.560E-02	0.516E-02	-.432E-02
τ_{33}	0.994	0.00	-.138E-01	0.00	-.107E-01
$\alpha_c = 0.93$	$C(E, M2)$	$E_{\max}$	$E_{\min}$	$M2_{\max}$	$M2_{\min}$
τ_{11}	0.970	0.00	-.315E-01	0.00	-.188E-01
τ_{12}	0.969	0.151E-01	-.130E-01	0.890E-02	-.854E-02
τ_{13}	0.975	0.168E-01	-.105E-01	0.105E-01	-.666E-02
τ_{22}	0.968	0.00	-.298E-01	0.00	-.210E-01
τ_{23}	0.975	0.133E-01	-.101E-01	0.900E-02	-.624E-02
τ_{33}	0.978	0.00	-.270E-01	0.00	-.162E-01
$\alpha_c = 0.45$	$C(E, M2)$	$E_{\max}$	$E_{\min}$	$M2_{\max}$	$M2_{\min}$
τ_{11}	0.861	0.00	-.445E-01	0.00	-.186E-01
τ_{12}	0.872	0.217E-01	-.201E-01	0.101E-01	-.911E-02
τ_{13}	0.887	0.252E-01	-.161E-01	0.138E-01	-.109E-01
τ_{22}	0.865	0.00	-.488E-01	0.00	-.285E-01
τ_{23}	0.890	0.217E-01	-.143E-01	0.974E-02	-.888E-02
τ_{33}	0.901	0.00	-.413E-01	0.00	-.226E-01

Table 4: Correlations between exact (E) residual fields τ_{kl} and their similarity modeled ($M2$) counterparts, and maximum and minimum values of E and $M2$ fields, for case of identical grid and test filters, whose parameter α_c is provided in upper left box of each block.

$(1.89, 1.77)$	$C(E, M1)$	$C(E, M2)$	$C(E, M3)$
τ_{11}	0.038	0.724	0.638
τ_{12}	0.105	0.727	0.668
τ_{13}	0.099	0.710	0.566
τ_{22}	0.046	0.723	0.630
τ_{23}	0.097	0.710	0.557
τ_{33}	0.173	0.700	0.428
$(1.71, \pi/2)$	$C(E, M1)$	$C(E, M2)$	$C(E, M3)$
τ_{11}	0.040	0.692	0.634
τ_{12}	0.111	0.694	0.664
τ_{13}	0.101	0.678	0.559
τ_{22}	0.049	0.692	0.626
τ_{23}	0.098	0.679	0.554
τ_{33}	0.176	0.674	0.425
$(1.37, 1.16)$	$C(E, M1)$	$C(E, M2)$	$C(E, M3)$
τ_{11}	0.044	0.599	0.621
τ_{12}	0.123	0.599	0.654
τ_{13}	0.102	0.583	0.550
τ_{22}	0.054	0.600	0.613
τ_{23}	0.098	0.587	0.545
τ_{33}	0.179	0.590	0.416
$(1.71, 1.16)$	$C(E, M1)$	$C(E, M2)$	$C(E, M3)$
τ_{11}	0.040	0.533	0.634
τ_{12}	0.111	0.532	0.664
τ_{13}	0.101	0.521	0.559
τ_{22}	0.049	0.531	0.626
τ_{23}	0.098	0.523	0.554
τ_{33}	0.176	0.529	0.425

Table 5: Correlations between exact (E) residual fields and their modeled (M) counterparts, for case with fourth-order grid filter and second-order test filter, whose respective cutoffs α_c are provided in upper left box of each block.

(1.16,1.71)	$C(E2, E4)$
τ_{11}	0.548
τ_{12}	0.548
τ_{13}	0.536
τ_{22}	0.546
τ_{23}	0.538
τ_{33}	0.544
Q_1	0.537
Q_2	0.539
Q_3	0.535

Table 6: Correlations between exact residual-stress components computed by second-order ($E2$) and fourth-order ($E4$) grid filtering, whose respective cutoffs α_c are given at upper left.

7 Discussion

In the conventional practice of LES, the grid filter and the SGS-model have often been treated as if they were independent choices (as observed by Piomelli et al. [16]). In contrast, a priori analyses with a continuously tunable filter reveal that the filter, the exact SGS stresses, and the model are closely interrelated. Thus, the filter and the model should not be specified independently.

For reasons of practicality, our computational study was limited to a single test flow at a relatively low Re_λ, much lower, for example, than the value $Re_\lambda = 310$ in the experiment of Liu et al. [4]. It is natural to wonder if the high correlations observed for the stress-similarity model ($M2$) generalize to other flows and to higher Re_λ. Several considerations suggest an affirmative answer. First, correlations of 0.85 were observed for $M2$ in the physical experiment of Liu et al. [4] whenever identical second-order grid and test filters were exploited. Second, by comparing Fig. 8 and Table 7 below, one observes some dependence of the correlation coefficient on Re_λ, but it appears to be relatively weak. Third, with identical second-order Pade grid and test filters each of $\alpha_c = \pi/2$, Adams et al. [17] have recently observed correlations well in excess of 0.90 for DNS of a forced turbulent Mach 3.0 boundary-layer flow along a compression ramp, for which Re_λ grows from a value of 47 in the incoming

t	$C(E, M2)$
.127	0.966
.287	0.971
.644	0.978
.829	0.982
.977	0.985
1.08	0.987
1.18	0.988
1.24	0.989
1.40	0.991
1.51	0.992

Table 7: Time evolution of correlation coefficients of the form $C(\tau_{11}, \mathcal{L}_{11})$ for identical grid and test filters with $\alpha_c = \pi/2$.

boundary layer to 326 midway up the compression ramp. Moreover, even with a much more dissipative filter ($\alpha_c = 0.53$), correlations on the order 0.8 are observed. It is important to note that, in contrast to the present test case, the flow considered by Adams et al. is highly anisotropic, highly compressible, and wall-bounded.

8 Conclusions

The decay of isotropic turbulence in a compressible flow is examined by direct numerical simulation (DNS). *A priori* analyses of the DNS data are then performed to evaluate three candidate subgrid-scale stress (SGS) models for large-eddy simulations (LES): the generalized (compressible) Smagorinsky model ($M1$) of Erlebacher et al. [8], the stress-similarity model ($M2$) of Liu et al. [4], and the generalized Clark model ($M3$) of Vreman et al. [7].

The focus of the study is an examination of the effect of the grid and test filters on the fidelity of the models. For this purpose, tunable, one-parameter filters of Pade type are exploited. Tunable filters are desirable for LES in that they allow the cutoff wavenumber k_c to be specified independently of the grid resolution Δx. In our view, the cutoff should be selected on the basis of physical considerations and the grid resolution on the basis of mathematical ones.

In the *a priori* analyses, the modeled residual stresses are correlated against their exact counterparts for selected values of the cutoff wavenumber k_c of the filter. On the basis of these results, the following conclusions are offered:

1. The distribution and the scale of the exact residual-stress tensor τ_{kl} depends strongly on both the cutoff k_c and the order property of the grid filter. This dependence is partially revealed by the simple recognition that the residual stresses must vanish entirely in the limit as $k_c \to k_\eta$, where k_η is the Kolomogorov wavenumber. Consequently, in general, no SGS-stress model can be independent of the grid filter. In particular, there is no universal Smagorinsky constant; the constant necessarily depends of the character of the grid filter.

2. Correlations of the form $C(E, M)$ between the exact (E) and modeled (M) SGS stresses are typically very high $(C > 0.9)$ for the stress-similarity model $(M2)$, moderately good $(C \approx 0.6)$ for the Clark model $(M3)$, and poor $(C < 0.2)$ for the Smagorinsky model $(M1)$.

3. For each of the three models, higher correlations $C(E, M)$ are observed for less dissipative grid filters and vice versa. This is an expected result because (for a fixed grid resolution) dissipative filters are characterized by relatively low cutoff wavenumbers k_c, which in turn results in more energetic subgrid scales of motion.

4. Model $M2$ performs remarkably well in *a priori* tests provided the grid and test filters have the same order property. The highest correlations, well in excess of 0.90, are obtained for $M2$ whenever the grid and test filters are identical. If the grid and test filters are identical *and* the filters are not too dissipative, model $M2$ appears to capture not only the correct distribution of stress but also the correct amplitude whenever the model constant $c_L = 1.0$. This result numerically replicates Bardina's [10] result, albeit for compressible flow.

5. The present results for models $M1$ and $M2$ are consistent with the experimental findings of Liu et al. [4], who did not consider $M3$.

20

6. Whereas models $M1$ and $M3$ appear to degrade whenever the flow is instantaneously anisotropic, model $M2$ appears relatively insensitive to anisotropy.

As a concluding thought, we acknowledge the well-known experience that both Bardina's model (e.g., Liu et al. [4]) and Clark's model (Vreman et al. [5]) are insufficiently dissipative for practical applications to LES. However, in our view, the physics and the mathematics of LES need decoupling. It appears increasing likely that stress-similarity models ($M2$, for example) capture the physics (e.g., backscatter) with high fidelity. That such models "blow up" in practice is not surprising in light of Fig. 1. The physical viscosity, which dampens the highest wavenumbers in DNS, is ineffective in LES at the cutoff wavenumber k_c. We conclude that the instability of similarity models is ultimately a mathematical issue, not a physical one.

Acknowledgments

21

Appendix: One-Parameter Pade Filters

Let $\mathbf{f}$ be a vector containing $n + 1$ values $f_i = f(x_i)$ obtained by sampling a continuous function $f(x)$ at a set of equally spaced nodes $x_i = x_0 + i\Delta x$, $i = 0, 1, ..., n$. Further let $\bar{\mathbf{f}} = L\mathbf{f}$ denote the vector of filtered values obtained by applying the linear filter L to $\mathbf{f}$. Here, we consider Pade filters, for which $L = M^{-1}E$, whereby $M\bar{\mathbf{f}} = E\mathbf{f}$, and M and E are banded matrices.

Second-Order Pade Filters

Following Lele [3], a second-order, one-parameter (ζ) Pade filter is constructed by considering the symmetric pointwise scheme

$$\zeta \bar{f}_{i-1} + \bar{f}_i + \zeta \bar{f}_{i+1} = af_i + \frac{b}{2}(f_{i-1} + f_{i+1}) \quad ; \quad (i = 1, 2, ...n - 1) \tag{29}$$

Various treatments are possible for the boundary nodes $i = 0$ and $i = n$. However, the simplest approach, sufficient for our present purposes, is to impose no filtering at the boundaries. For the second-order Pade scheme, M and E are tridiagonal matrices.

It is instructive consider the action of the filter of Eq. 29 on the single Fourier mode $\exp(\iota k x)$ ($\iota = \sqrt{-1}$), from which we obtain the complex *transfer function*

$$H(\alpha) = \frac{a + b\cos(\alpha)}{1 + 2\zeta\cos(\alpha)} \tag{30}$$

where $\alpha = k\Delta x$. For a fixed grid increment Δx, the transfer function defines the action of the filter on modes of wavenumber k. For applications to LES, we consider only *low-pass* filters, for which $H(0) = 1$ and $H(\pi) = 0$. In combination, these two constraints imply that $b = a = 0.5 + \zeta$. Admissible values of the parameter are $-\frac{1}{2} < \zeta \leq \frac{1}{2}$. Whenever $\zeta = 0$, M is the identity matrix, and the filter is said to be *fully explicit*. The fully explicit case corresponds to a discrete *top-hat* filter with weights at adjacent nodes of [1/4, 1/2, 1/4]. Otherwise, the filter is *implicit*. The value $\zeta = \frac{1}{2}$ yields $M = E$, which turns off the filter. For all admissible parameter values, the matrices M and E are diagonally dominant with positive diagonal elements, in which case the operator L is positive semidefinite.

By analogy to discrete differentiation operators, to each discrete filter is associated a Taylor-series expansion of the form

$$\bar{f}(x_i) = f(x_i) + a_1 \Delta x f'(x_i) + a_2 \Delta x^2 f''(x_i) + a_3 \Delta x^3 f'''(x_i) + ... \qquad (31)$$

Here, for notational simplicity, the factorials in the Taylor expansion have been absorbed into the coefficients a_j. By applying the Taylor-series representation of the filter to $\exp(\iota k x_i)$, we obtain the corresponding Taylor series of the transfer function, namely

$$H(\alpha) = 1 + a_1 \iota \alpha - a_2 \alpha^2 - a_3 \iota \alpha^3 + ... \qquad (32)$$

Equating successive derivatives of the two forms of the transfer function (Eqs. 30 and 32) at $\alpha = 0$, yields the coefficients a_j of the transfer function. Thus, the Taylor-series expansion of the filter implies the transfer function and vice versa. For the Pade filter of interest, the first two coefficients are

$$
\begin{aligned}
a_1 &= H'(0) = 0 \\
-2a_2 &= H''(0) = -\frac{1}{2} + \frac{2\zeta}{1 + 2\zeta}
\end{aligned}
\qquad (33)
$$

In general, a filter is said to be of order m if the first non-vanishing coefficient of its Taylor-series expansion is a_m. Thus, the Pade scheme is of second order (provided $\zeta \neq 0.5$). Equivalently, a filter is of order m if all derivatives of the transfer function of order less than m vanish at the origin. In general, filters associated with symmetric stencils (and coefficients) are of even order with purely real transfer functions. As a consequence, they filter without phase error.

As clearly indicated by Eq. 33, the coefficients of the Taylor-series expansions Eq. 31 and Eq. 32 are functions of the parameter. To quantify this dependence, we define α_c, the *cutoff wavenumber*, such that

$$C = H(\alpha_c) = \frac{(1 + 2\zeta)(1 + \cos \alpha_c)}{2(1 + 2\zeta \cos \alpha_c)} \qquad (34)$$

where $0 < C < 1$ but is otherwise arbitrary. (In signal processing, it is customary to define the cutoff such that $1/2 = |H(\alpha_c)|^2$.) Eq. 34 relates the original parameter ζ to the cutoff

wavenumber $0 < \alpha_c \le \pi$. The (unconventional) choice $C = 1/2$ yields the particularly useful relationship $2\zeta = -\cos(\alpha_c)$, which in turn yields

$$H(\alpha, \alpha_c) = \frac{(1 - \cos\alpha_c)(1 + \cos\alpha)}{2(1 - \cos\alpha_c \cos\alpha)} \tag{35}$$

Fig. 2 in Section 3 compares the transfer functions of the variable Pade filter for selected values of the cutoff α_c.

Fourth-Order Pade Filters

We adapt the three-parameter, symmetric, fourth-order filter of Lele [3] whose M and E matrices are penta- and hepta-diagonal, respectively. The pointwise scheme for nodes $i = 2, 3, ..., n - 2$ is

$$\beta\bar{f}_{i-2} + \zeta\bar{f}_{i-1} + \bar{f}_i + \zeta\bar{f}_{i+1} + \beta\bar{f}_{i+2} + = af_i + \frac{b}{2}(f_{i-1} + f_{i+1}) + \frac{c}{2}(f_{i-2} + f_{i+2}) + \frac{d}{2}(f_{i-3} + f_{i+3}) \tag{36}$$

where

$$\begin{aligned} a &= +(5 + 6\zeta - 6\beta + 16d)/8 \\ b &= +(1 + 2\zeta + 2\beta - 2d)/2 \tag{37} \\ c &= -(1 - 2\zeta - 14\beta + 16d)/8 \end{aligned}$$

$$\tag{38}$$

By enforcing $c = d = 0$, one arrives at a one-parameter, fourth-order filter whose matrices M and E are penta-diagonal and tridiagonal, respectively, and for which $\beta = (1 - 2\zeta)/14$. The stencil is closed by imposing no filtering at the boundaries and by using the explicit fourth-order formula below at the gridpoint adjacent to the boundary point.

$$\bar{f}_1 = \frac{3}{4}f_1 + \frac{1}{16}(f_0 + 6f_2 - 4f_3 + f_4) \tag{39}$$

An analogous formula is used at gridpoint $n - 1$. Admissible values of the parameter are $-\frac{2}{3} < \zeta \le \frac{1}{2}$. (Gerschgorin's theorem guarantees positivity only for $-\frac{3}{8} \le \zeta \le \frac{1}{2}$.) A linear relationship between the original parameter ζ and $-1 \le \cos(\alpha_c) < 1$ establishes $12\zeta = -[1 + 7\cos(\alpha_c)]$, which defines the cutoff wavenumber α_c in terms of ζ.

24

References

[1] P. Moin and J. Jimenez, "Large-Eddy Simulation of Complex Turbulent Flows," AIAA Paper No. 93-3099 (1993).

[2] O. V. Vasilyev, T. S. Lund, and P. Moin, "A General Class of Commutative Filters for LES in Complex Geometries," submitted to *J. Comput. Phys.* (1998).

[3] S. K. Lele, "Compact Finite Difference Schemes with Spectral-Like Resolution," *J. Comput. Phys.*, **103**, 16 (1992).

[4] S. Liu, C. Meneveau, and J. Katz, "On the Properties of Similarity Subgrid-Scale Models as Deduced from Measurements in a Turbulent Jet," *J. Fluid Mech.*, **275**, 83 (1994).

[5] B. Vreman, B. Geurts, and H. Kuerten, "Large-Eddy Simulation of the Turbulent Mixing Layer," *J. Fluid Mech.*, **339**, 357 (1997).

[6] R. A. Clark, J. H. Ferziger, and W. C. Reynolds, "Evaluation of Subgrid-Scale Models Using an Accurately Simulated Turbulent Flow," *J. Fluid Mech.*, **91**, 1 (1979).

[7] B. Vreman, B. Geurts, and H. Kuerten, "Large-Eddy Simulation of the Temporal Mixing Layer Using the Clark Model," *Theoret. Comput. Fluid Dynamics*, **8**, 309 (1996).

[8] G. Erlebacher, M. Y. Hussaini, C. G. Speziale, and T. A. Zang, "Toward the Large-Eddy Simulation of Compressible Turbulent Flows," *J. Fluid Mech.*, **238**, 155 (1992).

[9] B. Vreman, B. Geurts, and H. Kuerten, "Realizability Conditions for the Turbulent Stress Tensor in Large-Eddy Simulation," *J. Fluid Mech.*, **278**, 351 (1994).

[10] J. Bardina, J. H. Ferziger, and W. C. Reynolds, "Improved Subgrid Scale Models for Large Eddy Simulation," AIAA Paper No. 80-1357 (1980).

[11] M. D. Love, "Subgrid Modeling Studies with Burgers' Equation," *J. Fluid Mech.*, **100**, 87 (1980).

[12] G. A. Blaisdell, N. N. Mansour, and W. C. Reynolds, "Numerical Simulation of Compressible Homogeneous Turbulence," Report TF-50, Department of Mechanical Engineering, Stanford University (1991).

[13] D. Obrist, "Ein Pseudospektralverfahren zur direkten numerischen Simulation isotroper kompressibler Turbulenz," Diploma Thesis, Institut für Fluiddynamik, ETH Zürich (1997).

[14] J. H. Williamson, "Low-Storage Runge-Kutta Schemes," *J. Comput. Phys.*, **35**, 48 (1980).

[15] D. A. Compton and J. A. Eaton, "Development of Near-Wall Statistics in a Three-Dimensional Turbulent Boundary Layers," in *Three-Dimensional Boundary Layers*, ASME FED-Vol. 237 (1996).

[16] U. Piomelli, P. Moin, and J. H. Ferziger, "Model Consistency in Large-Eddy Simulation of Turbulent Channel Flow," *Phys. Fluids A*, **31**, No. 7, 1884 (1988).

[17] N. A. Adams, S. Stolz, A. Honein, K. Mahesh, "Analysis and Modeling of Subgrid Scales for Shock-Boundary-Layer Interaction," Proc. 1998 Summer Program, Center for Turbulence Research, NASA Ames Research Center and Stanford University, Stanford, California (1998).
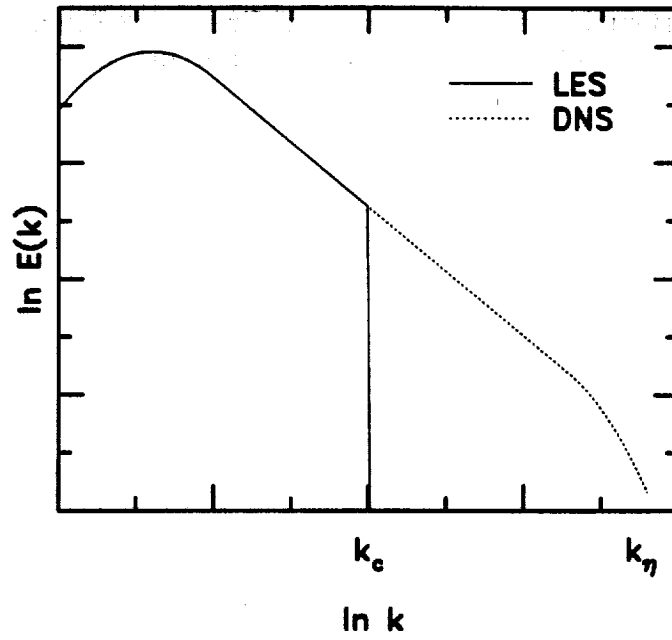
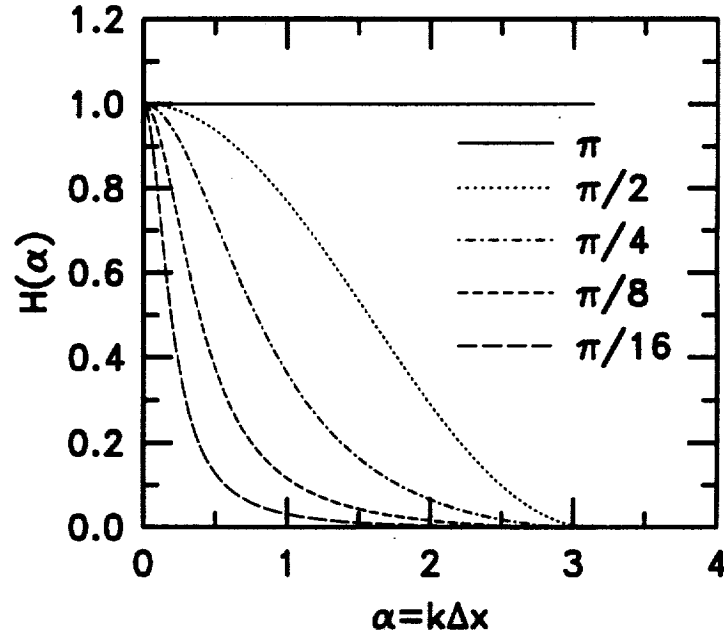Figure 1: Kolmogorov energy spectrum for idealized LES.

Figure 2: Transfer function of one-parameter family of second-order low-pass filters of Pade type for selected values of dimensionless cutoff wavenumber α_c.
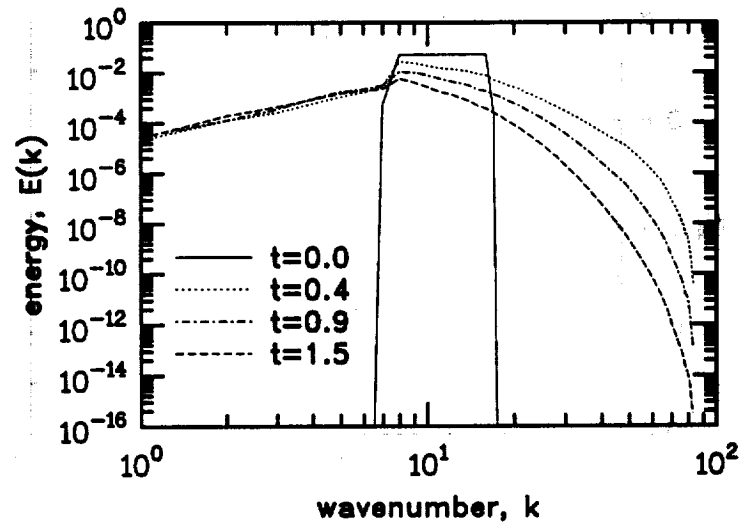
Figure 3: Kinetic energy spectrum at selected times
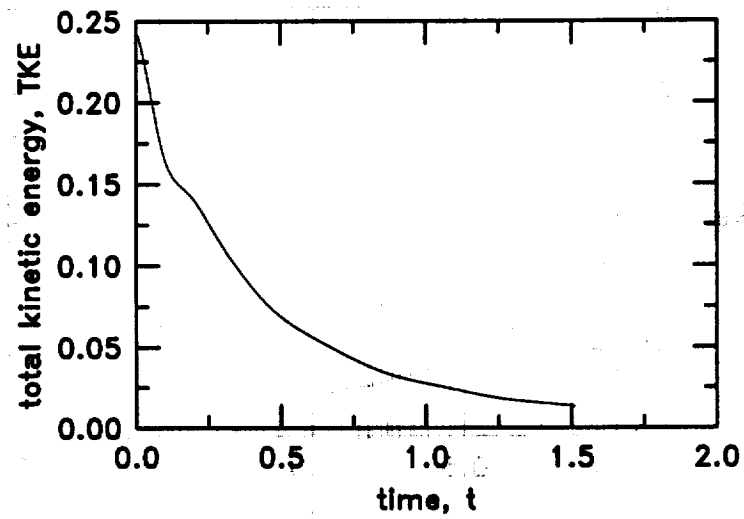
Figure 4: Temporal evolution of total kinetic energy TKE.
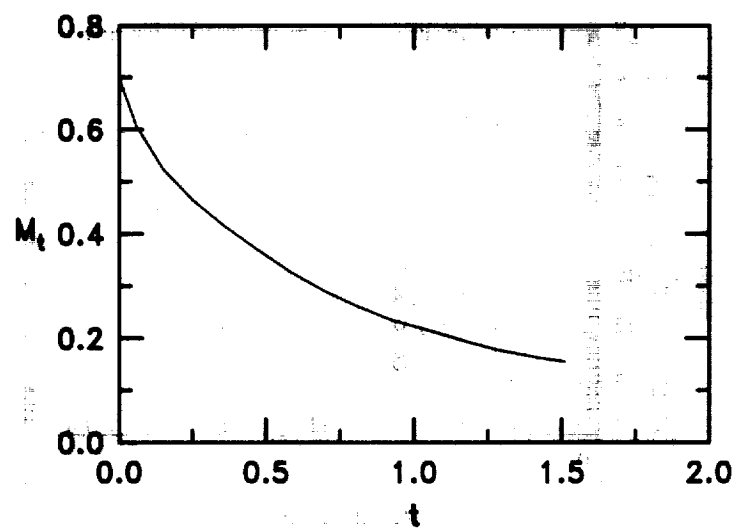
Figure 5: Temporal evolution of turbulent Mach number M_t.
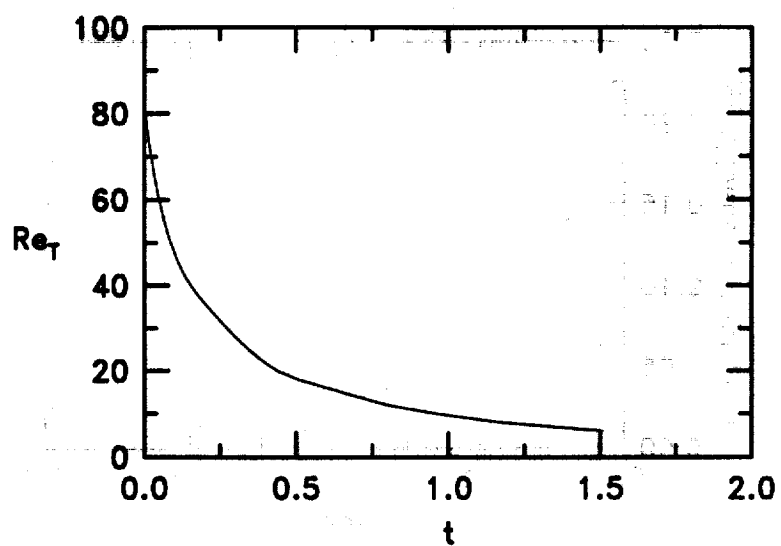
Figure 6: Temporal evolution of turbulent Reynolds number.
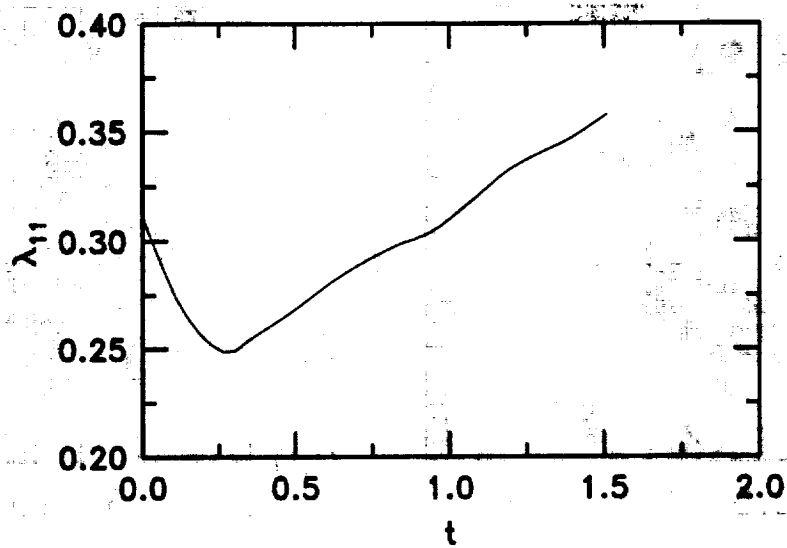
Figure 7: Temporal evolution of Taylor microscale λ_{11}.
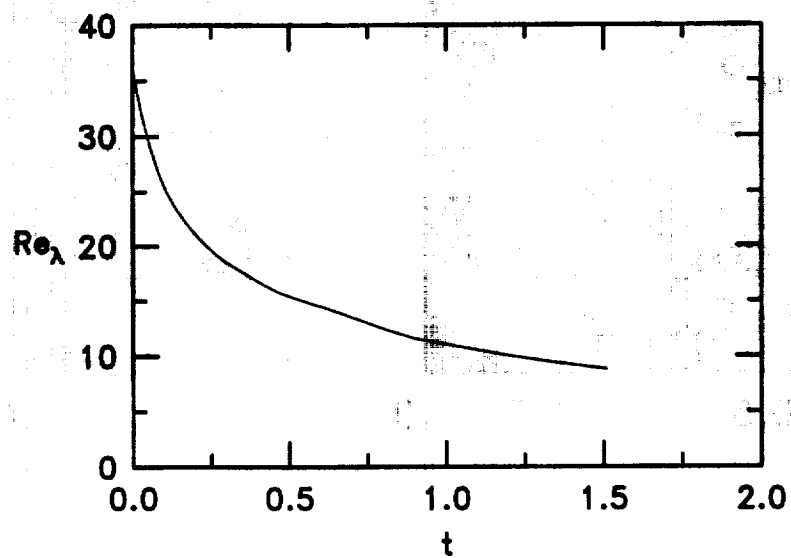
Figure 8: Temporal evolution of Taylor-microscale Reynolds number, Re_λ.
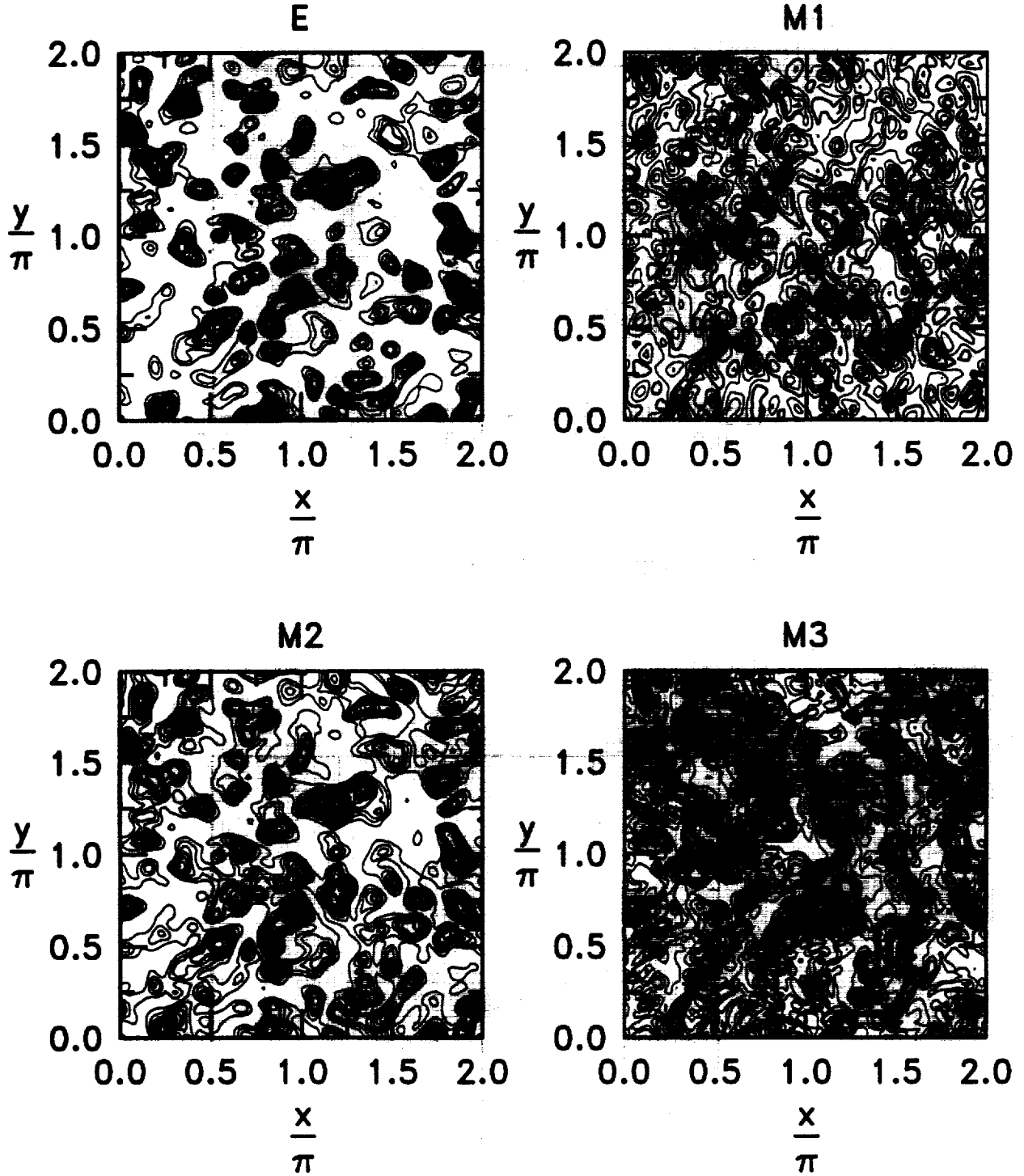
Figure 9: Contours of exact (E) and modeled (M) τ_{11} component of residual stress in selected $x - y$ plane at $t = 1.5$, for grid- and test-filter cutoff values $\alpha_c = \pi/2$ and $\alpha_c = 0.93$, respectively.

31
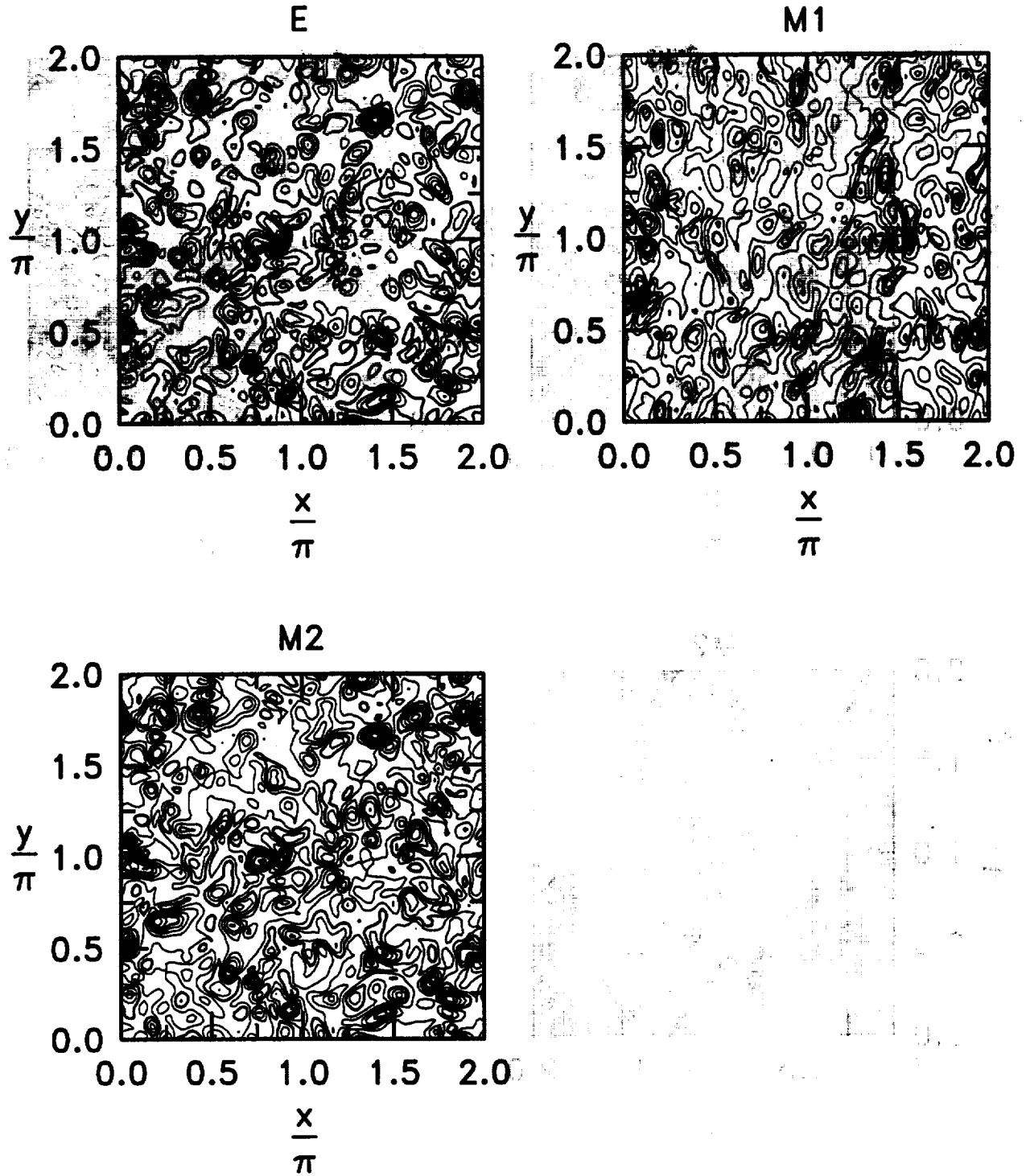
Figure 10: Contours of exact (E) and modeled (M) q_1 component of residual thermal stress in selected $x - y$ plane at $t = 1.5$, for grid-filter and test-filter cutoff values $\alpha_c = \pi/2$ and $\alpha_c = 0.93$, respectively.
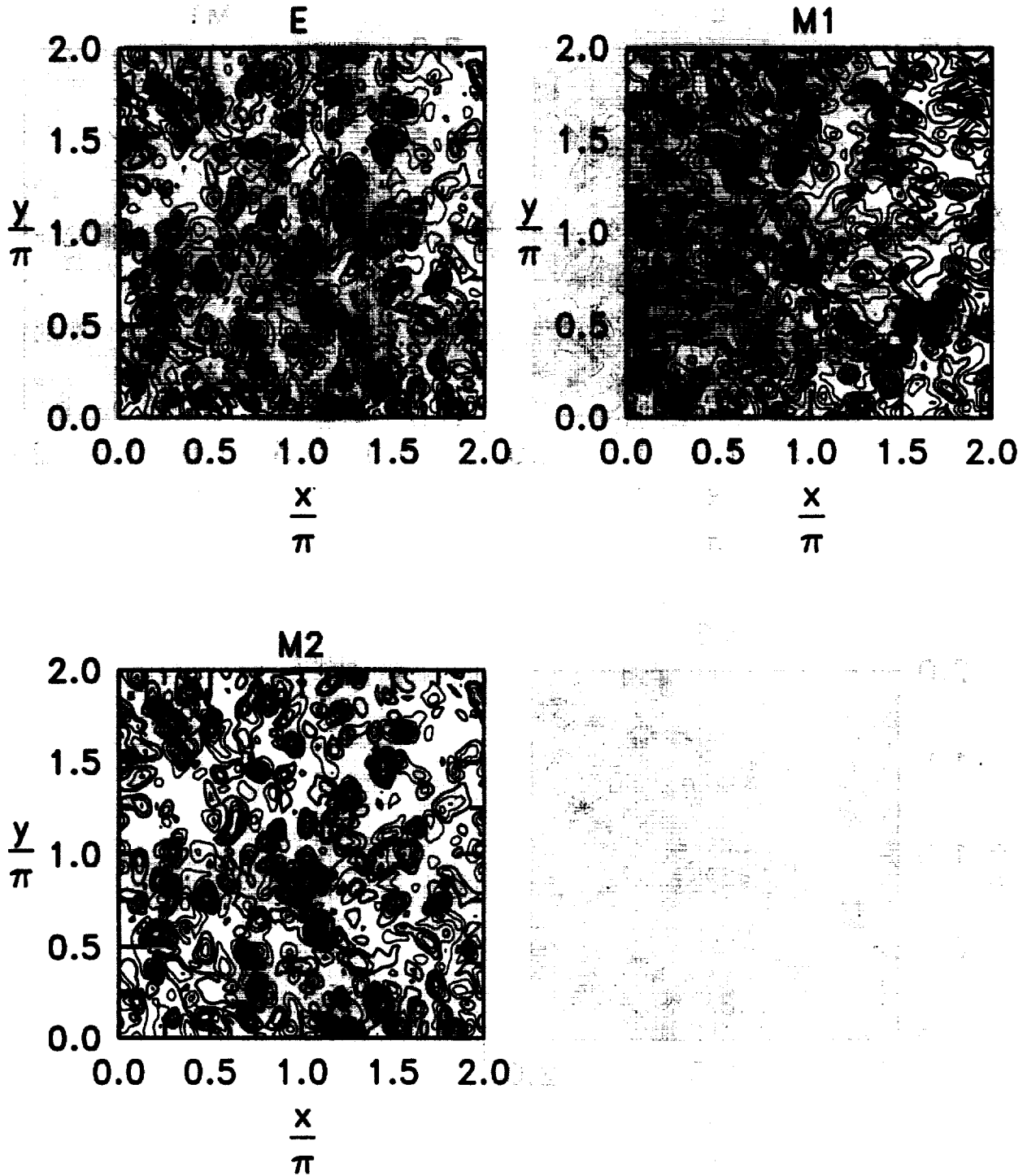
Figure 11: Contours of exact (E) and modeled (M) τ_{23} component of residual stress in selected $x - y$ plane at $t = 1.5$, for identical grid and test filters of cutoff values $\alpha_c = \pi/2$. For ranges of E and $M2$ values, see Table 4.

33
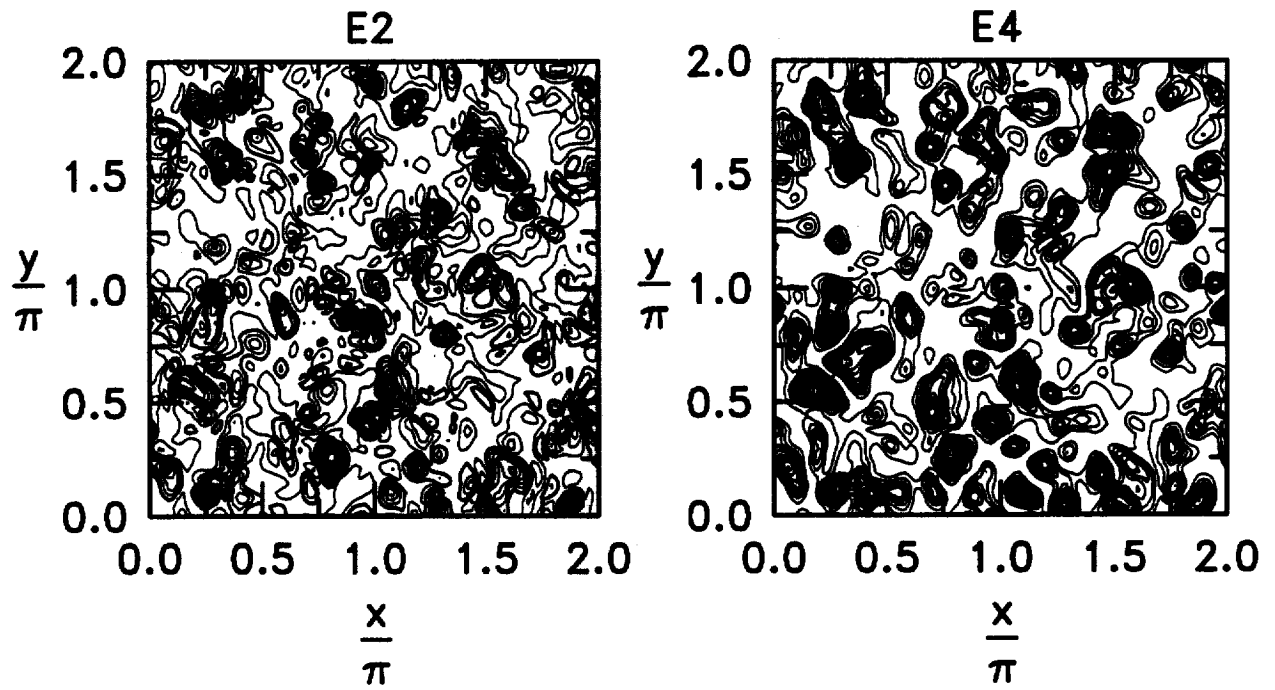
Figure 12: Comparison of exact (E) residual-stress component τ_{22} for grid filters of second $(E2)$ and fourth $(E4)$ order.